Computer-Aided Detection and Quantification of Intracranial Aneurysms

Tim Jerman, Franjo Pernuš, Boštjan Likar, and Žiga Špiclin

Faculty of Electrical Engineering, Laboratory of Imaging Technologies,
University of Ljubljana, Tržaška 25, 1000 Ljubljana, Slovenia
{tim.jerman,ziga.spiclin,bostjan.likar,franjo.pernus}@fe.uni-lj.si

Abstract. Early detection, assessment and treatment of intracranial aneurysms is important to prevent rupture, which may cause death. We propose a framework for detection and quantification of morphology of the aneurysms. A novel detector using decision forests, which employ responses of blobness and vesselness filters encoded in rotation invariant and scale normalized frequency components of spherical harmonics representation is proposed. Aneurysm location is used to seed growcut segmentation, followed by improved neck extraction based on intravascular ray-casting and robust closed-curve fit to the segmentation. Aneurysm segmentation and neck curve are used to compute three morphologic metrics: neck width, dome height and aspect ratio. The proposed framework was evaluated on ten cerebral 3D-DSA images containing saccular aneurysms. Sensitivity of aneurysm detection was 100% at 0.4 false positives per image. Compared to measurements of two expert raters, the values of metrics obtained by the proposed framework were accurate and, thus, suitable for assessing the risk of rupture.

Keywords: intracranial aneurysm, rupture, detection, multiscale enhancement, random forests, segmentation, neck extraction, morphology.

1 Introduction

The prevalence of intracranial aneurysms is between 2%-5% of the world population and, although aneurysm rupture is a rather rare event, the majority of patients that experience the rupture die of subarachnoid hemorrhage [3]. To prevent such fatal events, aneurysms should be detected, assessed and treated as early as possible. After an aneurysm is detected, the risk of rupture is assessed through quantitative studies of its morphology and hemodynamics so as to prioritize the treatment of patients. Quantifying the morphology of aneurysms can be performed manually using a 3D angiographic image like 3D digital subtraction angiography (3D-DSA). However, tasks like manual detection, segmentation, isolation and measurement of the aneurysm in a complex 3D vascular tree, usually based on observing 2D cross-sections of the 3D image, are tedious and time consuming to perform for a clinician. To assist the clinician, but also to improve the accuracy, reliability and reproducibility of the outcome [1], there is a need for computer-aided detection and quantification of the aneurysms.
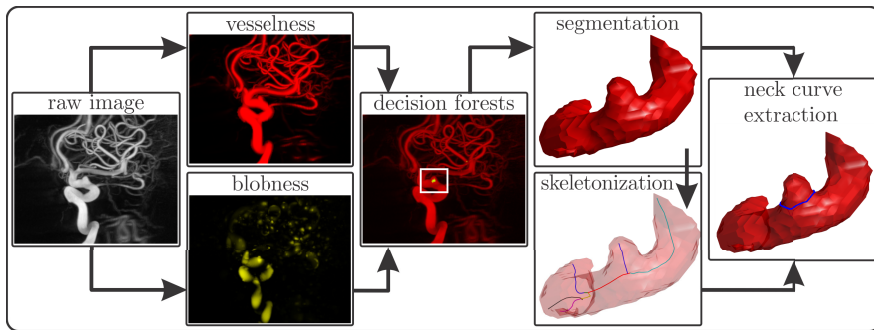
Fig. 1. Image analysis framework for aneurysm detection, segmentation and neck extraction based on a 3D angiogram.

Although several methods for detecting intracranial aneurysms [6,4], segmenting vascular structures [7] and extracting the aneurysm's neck curve [1], were proposed in the past, to the best of our knowledge, these methods still need to be further improved before being incorporated into a computer-aided detection and quantification framework. Of the aneurysm detection, segmentation, and quantification tasks, detection seems to be the most difficult. The specific hemodynamics of each aneurysm causes large variations of image intensity between different aneurysms, which, besides variations in aneurysm size and shape, adversely impact the performance of detection methods [6,4]. The intensity, size and shape variations typically result in lower sensitivity and specificity of computer-aided detection of aneurysms.

To aid the detection and quantification of intracranial aneurysms, we propose an image analysis framework that involves: a) enhancement of the 3D cerebral angiogram, b) novel detection of aneurysms based on random forests and rotation invariant and scale normalized visual features, c) a growcut segmentation of the aneurysm and attached vasculature, followed by d) neck curve extraction based on intravascular ray-casting to find points on the neck and a robust RANSAC-type closed-curve fitting. The proposed framework was evaluated on ten cerebral 3D-DSA images containing aneurysms, which were quantified by three morphologic metrics: neck width, dome height and aspect ratio. The achieved sensitivity of aneurysm detection was 100% at 0.4 false positives per image, while, compared to aneurysm measurements of two expert raters, the automatic measurements were accurate and thus suitable for assessing the risk of aneurysm rupture.

2   Methods

Main steps of the image analysis framework for the detection and morphologic quantification of cerebral aneurysms are illustrated in Fig. 1. The following subsections detail the aneurysm detection, segmentation and neck curve extraction. Based on aneurysm segmentation and neck curve, the morphologic metrics like neck width, dome height and aspect ratio of the aneurysm can be quantified.

2.1 Aneurysm Detection

Computer-aided detection of aneurysms in angiographic images should exhibit high sensitivity, but at the same time, reduce the number of false detections to a minimum. Since aneurysms are blob-like structures a simple approach to their detection is to employ blob enhancement on the images, e.g. multiscale filters based on analysis of Hessian eigenvalues [8]. Although the response of a blob enhancement filter is high at aneurysms and thus promising for computer-aided detection of aneurysms, the response may also be high at bifurcations and vessel bents, which, on a certain scale, resemble a blob-like structure. Hence, a blob enhancement filter will likely indicate many false positives (FPs). To better discriminate between the aneurysm regions, i.e. true positives (TPs), and other structures, and to further reduce FPs, we use random decision forests (RDFs) [2] trained on visual features obtained from the responses of enhancement filters.

Visual Features. For each location $\mathbf{x}_i \in \mathbb{R}^3$ in a 3D angiographic image $I(\mathbf{x})$ an ensemble of rotation invariant and scale normalized features that describe the local neighborhood of $\mathbf{x}_i$ are computed. First, the aneurysms and vessels of various sizes are enhanced by a multiscale Hessian-based filtering of $I(\mathbf{x})$ using blobness and vesselness [8] filters, with normalized responses denoted by $\mathcal{B}(\mathbf{x})$ and $\mathcal{V}(\mathbf{x})$, respectively. These two responses are locally resampled about $\mathbf{x}_i$ over concentric spheres (Fig. 2.b,c) parameterized by (θ, ϕ) and radii $r_k, k = 1, \dots, K$ and then projected onto spherical harmonics basis $Y_l^m(\theta, \phi)$ [5] to represent, e.g., the blobness response over a sphere as:

$$\hat{\mathcal{B}}(\theta, \phi | \mathbf{x}_i, r_k) = \sum_{l=0}^{L} \sum_{m=-l}^{m=l} a_{lm} Y_l^m(\theta, \phi), \tag{1}$$

where L is the maximal bandwidth of spherical basis functions m, and coefficients a_{lm} are computed from $\mathcal{B}(\theta, \phi | \mathbf{x}_i, r_k)$. Analoguously, we get $\hat{\mathcal{V}}(\theta, \phi | \mathbf{x}_i, r_k)$. A rotation invariant representation (Fig. 2.d) is obtained by computing the L_2-norm of spherical functions with respect to frequency l as [5]:

$$\hat{\mathcal{B}}_l^{i,k} = \left\| \sum_{m=-l}^{m=l} a_{lm} Y_l^m(\theta, \phi) \right\|, \tag{2}$$

where a simpler notation was used to indicate the dependence on $\mathbf{x}_i$ and r_k. Analoguously, we get $\hat{\mathcal{V}}_l^{i,k}$. To normalize the scale we first compute the rotation invariant features for K concentric spheres with $r_K = R$, where R is some fixed radius larger than the structures of interest, and estimate the cutoff radius r_C:

$$r_C \leftrightarrow C = \sup\{ k = 1, \dots, K : \hat{\mathcal{B}}_0^{i,k}/\overline{\mathcal{B}}^{i,k} \geq 0.75 \}, \tag{3}$$

where $\overline{\mathcal{B}}^{i,k} = [\sum_{l=0}^{L} \hat{\mathcal{B}}_l^{i,k}]^{1/2}$. Scale and rotation invariant features are then computed for K concentric spheres with the outer sphere of radius $r_K = 2 \cdot r_C$. Finally, the ensemble of visual features for point $\mathbf{x}_i$ is obtained as:

$$\phi(\mathbf{x}_i) = \{\hat{\mathcal{B}}_0^{i,k}, \dots, \hat{\mathcal{B}}_L^{i,k}, \hat{\mathcal{V}}_0^{i,k}, \dots, \hat{\mathcal{V}}_L^{i,k} : k = 1, \dots, K\}. \tag{4}$$
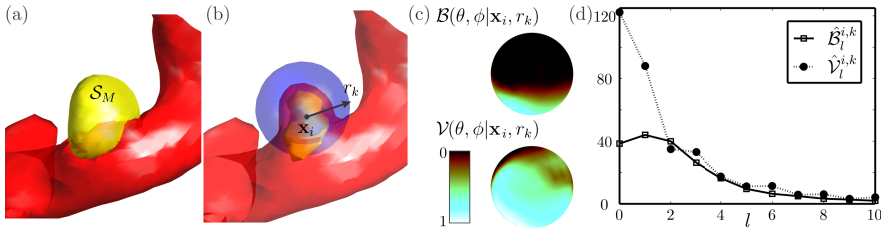
Fig. 2. (a) Reference segmentation $\mathcal{S}_M$ (yellow) of an aneurysm. (b) Blobness $\mathcal{B}(\mathbf{x}_i)$ and vesselness $\mathcal{V}(\mathbf{x}_i)$ sampled on a sphere with radius r_k around $\mathbf{x}_i$ are (c) projected onto a spherical harmonics basis, from which (d) rotation invariant features $\hat{\mathcal{B}}_l^{i,k}$ and $\hat{\mathcal{V}}_l^{i,k}$ are computed and used in a RDF based detector.

RDF Based Detector. RDF is trained on N angiographic images $I_n(\mathbf{x}); n = 1, \ldots, N$, in which the aneurysms were manually segmented by a neuroradiologist (Fig. 2). RDF requires visual features of two sets of points, one of TPs ($\mathcal{S}_{TP}$) and one of FPs ($\mathcal{S}_{FP}$). The set $\mathcal{S}_{TP}$ contains points with a high blobness response $\mathcal{B}(\mathbf{x}) > \tau_\mathcal{B}$ that lie within the manual segmentation $\mathcal{S}_M$ (Fig. 2.a), i.e. $\mathcal{S}_{TP} = \{\mathbf{x} : \mathbf{x} \in \mathcal{S}_M \wedge \mathcal{B}(\mathbf{x}) > \tau_\mathcal{B}\}$. Threshold $\tau_\mathcal{B}$ is manually determined. The set of FPs is obtained as $\mathcal{S}_{FP} = \{\mathbf{x} : \mathbf{x} \notin \mathcal{S}_{TP} \wedge \mathcal{B}(\mathbf{x}) > \tau_\mathcal{B}\}$. Since $\mathcal{B}(\mathbf{x})$ usually indicates many FPs, the cardinality of the two point sets may be unbalanced, i.e. $|\mathcal{S}_{TP}| \ll |\mathcal{S}_{FP}|$, thus points in $\mathcal{S}_{TP}$ are multiplied such that $|\mathcal{S}_{TP}| \approx |\mathcal{S}_{FP}|$.

Visual features are computed using (4) as $\{\phi(\mathbf{x}) : \mathbf{x} \in \mathcal{S}_{TP} \vee \mathbf{x} \in \mathcal{S}_{FP}\}$, while for each $\phi(\mathbf{x}_j)$ a class indicator variable $c(\mathbf{x}_j) \in \{\text{TP}, \text{FP}\}$ is set accordingly. The features are used to train a RDF of T independent trees Ψ_t; $t = 1, \ldots, T$ of depth D, in which information gain is maximized to determine optimal node splits [2]. The number of points in the training sets $\mathcal{S}_{TP}, \mathcal{S}_{FP}$ that reach a certain leaf is used to compute the posterior probabilities $p_t(c|\phi(\mathbf{x}))$ at each leaf in t-th tree.

Aneurysm detection on a test image $I(\mathbf{x})$ proceeds by extracting a set of candidate points $\mathcal{S}_{CP} = \{\mathbf{x} : \mathcal{B}(\mathbf{x}) > \tau_\mathcal{B}\}$. For each $\mathbf{x}_j \in \mathcal{S}_{CP}, j = 1, \ldots, |\mathcal{S}_{CP}|$ we compute the ensemble of visual features $\phi(\mathbf{x}_j)$ and then evaluate and average the posterior probabilities over all trees as:

$$p(c = \text{TP}|\phi(\mathbf{x}_j)) = \mathcal{L}(\mathbf{x}_j) = \frac{1}{T}\sum_{t=1}^{T} p_t(c = \text{TP}|\phi(\mathbf{x}_j)), \qquad (5)$$

where $\mathcal{L}(\mathbf{x}_j)$ is the aneurysm likelihood map. For a fixed threshold $0 < \tau_A < 1$, the set of points within aneurysms is detected as $\mathcal{S}_A = \{\mathbf{x} : \mathcal{L}(\mathbf{x}) > \tau_A\}$.

### 2.2   Aneurysm Segmentation and Neck Extraction

Based on a local segmentation of the aneurysm, intravascular ray-casting from the center of aneurysm to the vessel wall is used to find points on the aneurysm neck as the points with a high gradient in ray distance map. These points are fitted with a closed-curve to obtain the neck curve and isolate the aneurysm's dome, which is used to quantify the aneurysm.
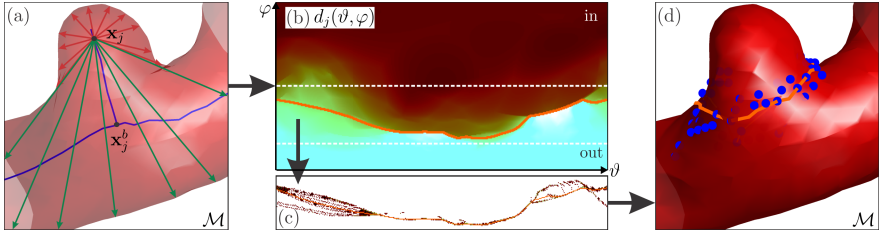
Fig. 3. (a) Intravascular ray-casting from the centerlines to segmentation surface $\mathcal{M}$ yields (b) distance maps $d_j(\vartheta,\varphi)$. (c) The edges in (b) are tentative points on the neck, which are used in a RANSAC-type fitting of closed-curve to obtain the final neck curve.

Segmentation of each aneurysm and neighboring vessels is performed by grow-cut [9], which requires seed points within the vascular structures and on background. First, the center $\mathbf{x}^c$ of each aneurysm is set as the center of the corresponding connected component in $\mathcal{S}_A$. Each $\mathbf{x}_j^c \in \mathcal{S}_A$ is merged to corresponding connected component in $\{\mathbf{x} : \mathcal{B}(\mathbf{x}) > \tau_{\mathcal{B}}\}$ to obtain a volume of interest (VOI) $\mathcal{S}_{j,VOI}$, set twice the size of bounding box of the connected component. Seeds within the vascular structures $\mathcal{S}_{j,+}$ are the 6-connected neighboors of $\mathbf{x}_j^c$, while seeds $\mathcal{S}_{j,-}$ on background are points within the VOI with low blobness and low vesselness response, i.e. $\{\mathbf{x} : ero(\mathcal{V}(\mathbf{x})) < \tau_{\mathcal{V}} \wedge \mathcal{B}(\mathbf{x}) < \tau_{\mathcal{B}}) \wedge \mathbf{x} \in \mathcal{S}_{j,VOI}\}$, where ero denotes binary erosion. Using the segmentation of vascular structure we extract its centerlines [7] and choose the aneurysm's centerline $\mathcal{S}_l$ as the centerline closest to $\mathbf{x}_j^c$ and then find a bifurcation point $\mathbf{x}_j^b$ connecting the aneurysm's centerline to the feeding vessel.

Extraction of aneurysm's neck curve is based on casting rays from $\mathbf{x}_j^c$ [10] in directions defined by $\vartheta \in [-\pi, \pi]$, $\varphi \in [0, \pi]$ towards the surface mesh $\mathcal{M}$ of the segmented vascular structures, measuring the ray distance to intersection and thresholding a corresponding distance map $d(\vartheta, \varphi)$. The idea is that between rays intersecting the neck (Fig. 3.a red) and those passing through the neck aperture (Fig. 3.a green), the distance increases noticeably. While the original method [10] is not robust to initial source point and thus requires user interaction, we perform ray casting from several points $\mathbf{x}_j \in \mathcal{S}_l$ with respect to $\mathbf{x}_j^b$ and then map the corresponding $d_j(\vartheta, \varphi)$ into a common coordinate frame (Fig. 3.b). A tentative neck curve is computed for each $d_j(\vartheta, \varphi)$ by initial Otsu thresholding and level set based segmentation determining the edge between the vessel and the aneurysm. All edges are mapped into common distance map and a 1D median filter is applied along φ (Fig. 3.c). The obtained points are projected onto $\mathcal{M}$, yielding possible neck curve points $\mathcal{C}$ (Fig. 3.d). The points in $\mathcal{C}$ are binned according to ϑ, with the bin size $\Delta\vartheta$. Using a RANSAC-type method, in which multiple subsets of points $\mathbf{x} \in \mathcal{C}' \subset \mathcal{C}$ are randomly selected by drawing at least one point from each bin, and then connected by shortest path across $\mathcal{M}$, the final neck curve is determined by subset $\mathcal{C}'$ that yields the shortest neck curve (Fig. 3.d).
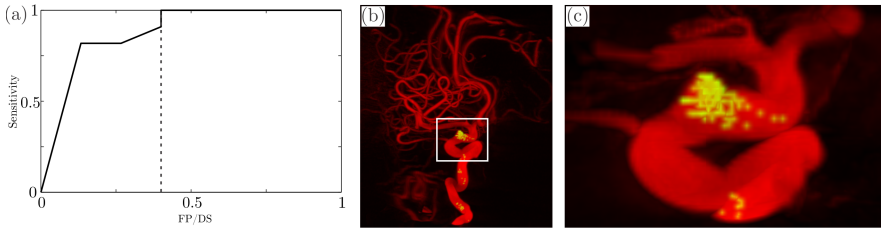
Fig. 4. (a) Free-response ROC curve of the RDF-based aneurysm detector showing sensitivity versus false positives per dataset (FP/DS) and (b,c) a maximum intensity projection of 3D-DSA with superimposed aneurysm likelihood map $\mathcal{L}(\mathbf{x}_j)$.

3   Experiments and Results

The proposed framework for the detection, segmentation, and neck curve extraction of cerebral aneurysms was trained on cerebral 3D-DSAs of $N = 15$ patients containing at least one intracranial saccular aneurysm. Another ten 3D-DSA images containing 15 intracranial saccular aneurysms were used for evaluation of the aneurysm detection, segmentation and neck curve extraction methods.

The RDFs were constructed with $T = 10$ trees of depth $D = 10$. For training and testing the RDFs we used points $\mathbf{x}$ with blobness $\mathcal{B}(\mathbf{x})$ above $\tau_{\mathcal{B}} = 0.15$. The visual features for RDFs were computed on $K = 10$ spheres with radii r_k increasing in equidistant steps. The maximum radius was $R = 10$, while the spherical harmonics bandwidth was set to $L = 15$. These parameters were determined by maximizing the overall detection performance on the test images.

The neck curve extraction was evaluated on 15 aneurysms from the test dataset. For evaluation, the neck curve was manually delineated by two experts on the surface of segmented aneurysm. Intravascular ray-casting was performed from 10 skeleton points $\mathbf{x}_j \in \mathcal{S}_l$ to obtain distance maps $d_j(\vartheta, \varphi)$.

Sampling of the tentative neck points used bin size of $\Delta\vartheta = 30°$. To quantitatively compare the neck curves extracted manually and automatically, we computed three morphologic metrics of the aneurysms: average neck width (NW), dome height (DH), and aspect ratio: $AR = DH/NW$. AR has been studied widely and has consistently been found to correlate with risk of aneurysm rupture [3].

Results. For each of the 10 test images, the aneurysm likelihood map $\mathcal{L}(\mathbf{x})$ was computed and thresholded with τ_A to obtain points $\mathcal{S}_A$ on aneurysms, whereas connected components smaller than 15 voxels were eliminated. The sensitivity and the amount of false positives per dataset (FP/DS) were determined at various threshold values $0 < \tau_A < 1$ so as to obtain the free-response receiver operating characteristic (FROC) curve shown in Fig. 4.a. The proposed detection method achieved a 100% sensitivity at 0.4 FP/DS. A maximum intensity projection (MIP) of a test image is shown in Fig. 4.b, in which the yellow component represents the superimposed aneurysm likelihood map with values above $\tau_A = 0.5$. The aneurysm location is clearly visible as a cluster of points (Fig. 4.c).

Fig. 5 shows Bland-Altman diagrams with the bias and standard deviation (SD) of error of NW, DH and AR measures between the two expert raters and
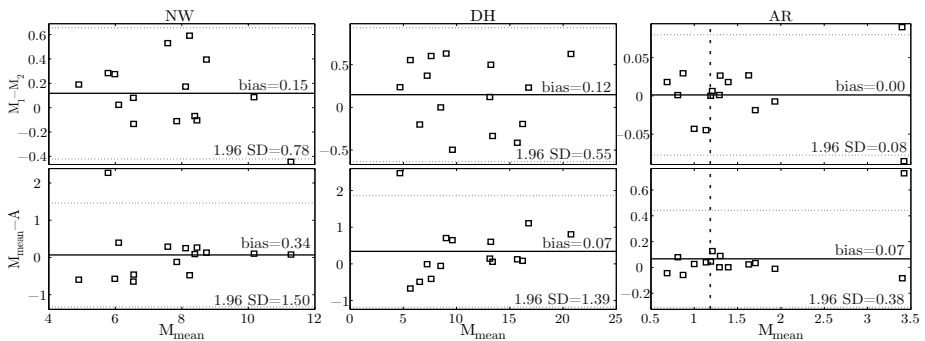
Fig. 5. Bland-Altman diagrams of quantitative aneurysm measures: average neck width (NW), dome height (DH) and aspect ratio (AR=H/NW), computed from two expert (M) and one automatic (A) neck curve delineations. Aneurysms with AR>1.18 (vertical dashed line) have a high risk of rupture [3].

between averaged values of the two raters and values obtained by the proposed neck extraction method. The agreement between the two raters was high as the bias and the SD were low, while in the comparison between the raters and the proposed method bias was low, but SD was slightly higher. The SD was higher because of one small aneurysm that had a low curvature on the neck, thus, the neck curves of both the expert raters and the automatic method differed substantially. Ignoring this outlier reduced the bias and SD of AR to 0.02 and 0.11, which is similar to the values obtained between the raters.

4 Discussion

To assist the clinician, we proposed a framework for computer-aided detection and morphologic quantification of cerebral aneurysms that involves a novel detection approach, local aneurysm segmentation, and improved neck curve extraction of intracranial aneurysms. The segmentation and neck curve are used for aneurysm isolation and quantification of its morphology, which is important for assessing the risk of rupture and planning the treatment.

The proposed aneurysm detection is based on random decision forests, which employ novel visual features based on responses of blob and vessel enhancement filters [8], Locations with high blobness are considered in feature extraction that proceeds by sampling the two response maps over concentric spheres, which are encoded by rotation invariant and scale normalized spherical harmonics. Thereby, characteristic aneurysm shape is encoded, while the variability, non-informative for the detection, is minimized. On ten 3D-DSAs containing 15 aneurysms, the proposed method achieved a 100% sensitivity at 0.4 FP/DS.

Although the results of other methods were obtained on other datasets, and are thus not directly comparable, their performance is slightly worse with 95% at 2.6 FP/DS [4] and 100% at 0.66 FP/DS [6]. Moreover, Lauric et al. [6] require a highly accurate segmentation of the entire vasculature, which is difficult to

obtain because of intensity variations of the 3D-DSA [7]. Herein the proposed framework executes a VOI-based aneurysm segmentation [9] after the detection.

To robustly isolate and quantify the aneurysm, we improved neck curve extraction by repeated intravascular ray-casting [10] to sample neck edge points, to which a closed-curve was fit by a RANSAC-type approach. Validation was performed by observing the bias and standard deviation of three morphologic measures of the aneurysms, i.e. NW, DH, AR, with respect to manual delineations of two expert raters (Fig. 5). Except for one small aneurysm, in which the extracted neck curve substantially differed from manual delineations, the computed measures were consistent over all aneurysms.

Aspect ratio (AR) is widely used as a measure of risk rupture [1], thus the methods for its assessment need to be accurate and reproducible. For aneurysms with AR>1.18 (dashed vertical line in Fig. 5) the risk of rupture is considered high, thus an immediate treatment is required [3]. Compared to four methods analyzed on a different database of aneurysms in [1] that had a mean relative error of 9.1, 7.5, 6.9, and 6.8% of AR versus a manual reference, the proposed method had the lowest mean relative error of 5.2%. Hence, the obtained low mean relative error renders the proposed method highly suited for assessing the risk of aneurysm rupture. Evaluation of the proposed framework shows encouraging results on 3D-DSA images. Since aneurysm detection and isolation rely on highly sensitive blob and vessel enhancement filters the approach also seems promising for other angiographic modalities like CTA and MRA.

References

1. Cardenes, R., Larrabide, I., et al.: Performance assessment of isolation methods for geometrical cerebral aneurysm analysis. Med. Biol. Eng. Comput. 51(3) (2012)
2. Criminisi, A., Shotton, J. (eds.): Decision Forests for Computer Vision and Medical Image Analysis. Springer, London (2013)
3. Dhar, S., Tremmel, M., Mocco, J., et al.: Morphology Parameters for Intracranial Aneurysm Rupture Risk Assessment. Neurosurgery 63(2), 185–197 (2008)
4. Hentschke, C.M., Beuing, O., Paukisch, H., et al.: A system to detect cerebral aneurysms in multimodality angiographic data sets. Med. Phys. 41(9), 091904 (2014)
5. Kazhdan, M., Funkhouser, T., Rusinkiewicz, S.: Rotation invariant spherical harmonic representation of 3D shape descriptors. In: Proc. Symp. on Geom. Proc. (2003)
6. Lauric, A., Miller, E., Frisken, S., et al.: Automated detection of intracranial aneurysms based on parent vessel 3D analysis. Med. Image. Anal. 14(2), 149–159 (2010)
7. Lesage, D., Angelini, E.D., et al.: A review of 3D vessel lumen segmentation techniques: Models, features and extraction schemes. Med. Image Anal. 13(6) (2009)
8. Sato, Y., Westin, C.-F., et al.: Tissue classification based on 3D local intensity structures for volume rendering. IEEE T. Vis. Comput. Gr. 6(2), 160–180 (2000)
9. Vezhnevets, V., Konushin, V.: Growcut - interactive multi-label n-d image segmentation by cellular automata. In: Proc. GraphiCon (2005)
10. van der Weide, R., Zuiderveld, K., Mali, W.P.T.M., et al.: CTA-based angle selection for diagnostic and interventional angiography of saccular intracranial aneurysms. IEEE Trans. Med. Imag. 17(5), 831–841 (1998)